Available online at www.sciencedirect.com

ScienceDirect

Journal of Ocean Engineering and Science 3 (2018) 156–174

www.elsevier.com/locate/joes

Water entry and exit of axisymmetric bodies by CFD approach

Vinod V. Nair, S.K. Bhattacharyya*

Department of Ocean Engineering, Indian Institute of Technology Madras, Chennai 600036, India

Received 14 December 2017; received in revised form 4 May 2018; accepted 7 May 2018
Available online 15 May 2018

Abstract

The water impact and subsequent entry of three rigid axisymmetric bodies, a sphere and two cones, in the early phase are simulated using CFD utilizing a VOF scheme to track the free surface and the results compared with the recent experimental results available in the literature. The penetration depth, vertical velocity and vertical acceleration time histories have been reproduced well by CFD with a wide choice of mesh density, whereas the peak pressure on impact required a much finer mesh and appropriate choice of the time step. Delineating an interaction region around the trajectory of the body with fine mesh and an adaptive time stepping strategy has worked well to capture the peak impact pressure accurately with reasonable computational effort.

The 'full' motion of the sphere, which is buoyant, has also been simulated using CFD allowing its 6-dof motion for several cycles of entry and exit phases. The features of the behavior, especially the loss of symmetry of the trajectory, are discussed.

Keywords: CFD; Cone; Sphere; Water entry; Water impact.

1. Introduction

Water entry of rigid bodies is an important area of research which has many marine applications. The slamming of ships, where the bow comes out of the sea surface and then slams back on to it, induces high local loads on the ship structure. A high frequency of the slamming event often leads to structural failure. Re-entry vehicles or manned space capsules landing in the sea must withstand the high loads that are generated by their impact on the sea surface at high velocities. The problem of water impact and subsequent entry of solid objects below the water surface, therefore, is of interest in the design of torpedoes, missiles, seaplanes, ships, free fall of lifeboats, flying boats etc. Such water entry problems require reliable prediction of the displacements, velocities, accelerations and the peak pressure loads on the structure. Fluid dynamic phenomena of jet formation, cavity formation behind the body, and splashing of water happen during water entry of a blunt body.

The very first literature reported on the problem of water impact of rigid bodies was by von Karman [24], in which an analytical expression was given for the force of impact which was derived from the momentum theorem without considering the effect of the rise of the water surface (generally termed as the effect of splash up) when the body enters water. The rise in water surface and its effect on impact force was considered by Wagner [25] where it was shown that the rise of the water surface leads to an increase in the impact force. Even though several decades of research has been done in this area, Wagner's approach still remains a benchmark for water impact problems.

A number of experiments have been reported in the literature on the water entry of bodies of various shapes such as hemisphere, sphere, cone, wedge, horizontal cylinder, ship type bow flare section etc. This paper considers two shapes, namely, the sphere and cone. Chuang and Milne [6] conducted drop tests of cones (16 in. or 0.4064 m diameter at base) with deadrise angles of 1°, 3°, 6°, 10° and 15° and reported that the impact pressures were generally much lower than the predictions by Wagner's theory and also concluded that the air entrapment on impact is negligible for cones with deadrise angles 3° and above. This work mainly

* Corresponding author.
E-mail address: skbh@iitm.ac.in (S.K. Bhattacharyya).

https://doi.org/10.1016/j.joes.2018.05.002

concentrated on maximum impact pressure as a function of touchdown (or, entry) velocity. May [15] conducted drop test on steel spheres (1/2 in. or 0.0127 m diameter) with focus on the cavity dynamics associated with water entry. Nisewanger [18] conducted drop tests on sphere (12 in. or 0.3048 m diameter) and measured the variation of pressure with respect to time and penetration depth. Baldwin [5] experimentally investigated the water entry of cones with deadrise angles 20–85° with focus on the variation of total drag and added mass with cone angle and penetration depth during water entry. Peseux et al. [20] measured the time variation of pressure by performing drop tests with both rigid and deformable cones (0.32 m base diameter) with deadrise angles 6°, 10° and 15° and compared the results with predictions by the finite element method (FEM). Alaoui et al. [2] carried out constant velocity experiments on hemisphere (0.392 m diameter) and cones (0.33 m base diameter) and measured the hydrodynamic loads and slamming coefficient during the impact. Alizadeh et al. [3] reported the penetration and velocity variation with time using high speed camera images of water impact by conducting drop test with a sphere (2.89 in. or 0.0734 m diameter) and compared the results with CFD simulation. De Backer et al. [7] performed drop test experiments on hemisphere (0.3 m diameter) and cones (0.3 m base diameter) with deadrise angles 20° and 45° and reported the variation of impact pressure, penetration depth, velocity and acceleration during the impact using high speed camera images and accelerometer based measurements during the water entry of all three models.

The water entry of rigid bodies has been studied analytically based on Wagner's theory and asymptotic solutions have been found for bodies of various shapes. Analytical study of water entry problem started with von Karman [24] and Wagner [25], and continued much later by Miloh [16], Greenhow [11] and Zhao and Faltinsen [31]. An extensive review of the slamming studies was reported by Korobkin and Pukhnachov [13].

Even though a great deal of progress has been made in this area, difficulties arise when there is a high deformation of the free surface or when the free surface breaks. These difficulties can be accounted for by Computational Fluid Dynamics (CFD) approach which involves solution of the Navier–Stokes equations by incorporating Volume of Fluid (VOF) method or some other free surface tracking methods. Kleefsman et al. [12] studied two dimensional (2D) water impact problems for wedge and horizontal cylinder and three dimensional (3D) impact problem for cone using the VOF method with finite volume discretization and had compared the variation of slamming coefficient with penetration depth but did not provide any result for the impact pressures. Shen and Wan [21] simulated the water entry of sphere (1 m diameter) using Open FOAM code coupled with the VOF and dynamic mesh method and presented the variation of displacement and also hydrodynamic forces. Fairlie-Clarke and Tveitnes [8] also used finite volume discretization with VOF method to track the free surface for simulating the constant velocity water entry of 2D wedges with various deadrise angles. Lin [14] developed a 2D model to simulate water entry as well as water exit of cylinders in a fixed grid system by incorporating cut cell technique into the VOF model and solving the RANS equations. Zhu et al. [32] used the Constrained Interpolation Method (CIP) to track the free surface to study the water entry and exit of horizontal cylinders. The variations of the slamming coefficient and penetration depth were reported for water entry at a constant velocity as well as under free fall. Yang and Qiu [28] used the CIP method to simulate the water entry of a 2D wedge, horizontal cylinder and catamaran section. Zhang et al. [30] used the level set method to simulate water entry and exit of cylinder and water entry of wedge. The variation of the slamming coefficient with penetration depth for cylinders, variation of velocity, vertical slamming force and pressure distribution for wedges were presented and compared with numerical and experimental results. Yang and Stern [29] used the level set method for simulating the water entry and exit of 2D cylinders. Aquelet et al. [4] simulated the water entry of wedges using the FEM in conjunction with the Arbitrary Lagrangian Eulerian (ALE) method for fluid-structure coupling. The pressure distribution and force variation were reported and compared with the theoretical values. Stenius et al. [23] simulated water entry of three dimensional (3D) wedge using the FEM and plotted the pressure variations. Wang and Soares [26] used explicit FEM to study the water impact of a hemisphere (0.3 m diameter) and cones (0.3 m base diameter) with deadrise angles 20°, 30°and 45° and reported the variation of penetration depth, velocity, acceleration, pressure distribution and impact coefficient and compared their results with experimental results. Meshless methods such as Smoothed Particle Hydrodynamics (SPH) have been used to investigate the water entry of rigid bodies in Oger et al. [19] and Gong et al. [10]. Maruzewski et al. [17] studied the water impact of a sphere (2 m diameter) and a ship hull section using the SPH and validated the variation of impact coefficient of the sphere and variation of force for the ship hull section by comparing them with experimental results. An extensive review of water entry dynamics with application to hull slamming is by Abrate [1], which also deals with CFD techniques in water entry problem.

From the above discussion, it is seen that there had been five papers on experimental drop tests with spheres (or hemispheres), namely, May [15] who studied only cavity behavior, Nisewanger [18] who reported only pressure distribution around the sphere, De Backer et al. [7] who presented penetration depth (i.e. vertical displacement), velocity, acceleration and pressure time histories, Alizadeh et al. [3] who presented displacement and velocity time histories and Alaoui et al. [2] who presented forces and related impact coefficient for water entry at constant speed. On the other hand, there are three papers treating the sphere entry problem using either CFD or FEM, namely, Alizadeh et al. [3] and Shen and Wan [21], both using CFD in conjunction with the VOF tracking method and Wang and Soares [26] using explicit FEM.

The present work adopts a CFD approach to the water entry problem of a sphere and two cones, all rigid, by solving the Navier–Stokes equations in conjunction with VOF

scheme to track the free surface. The results are compared with the recently published accurate measurements reported in De Backer et al. [7]. Unlike the work of Wang and Soares [26], who used the FEM to predict the same experimental results, the present paper uses the CFD approach, which, as will be brought out later, admits much larger time steps for accurate results and hence lower computational effort. Further, the experimental work of De Backer et al. [7] and its FEM validation by Wang and Soares [26] focus on early time when about 15% of the sphere diameter penetrates below the water surface. In this paper, however, the entire motion time history of the sphere, which is buoyant, in the entry (downward motion) phase as well as the rebound or exit (upward motion) phase followed by several oscillations (downward followed by upward motions) is also computed. The variations of penetration depth, velocity, impact pressure etc. are reported for different touchdown velocities along with their comparison with the experimental results.

2. CFD theory

A commercial CFD solver [9] has been chosen for the present study which uses a fixed mesh method for general moving object (GMO) and hence eliminating the complexities of moving mesh and deforming mesh. The conventional CFD solver mainly depends on deforming or moving mesh to accommodate moving objects. The moving and deforming mesh places a limitation on the distance between the object and the water in the context of water entry problem. Also, the simulation fails if the mesh deformation is too large. Remeshing and automatic mesh regeneration after certain time steps helps to address a few complexities in this regard but it becomes computationally expensive.

The GMO model uses the FAVOR (Fractional Areas/Volume Obstacle Representation) based technique to describe the geometric objects in the simulation domain by making use of area fraction (AF) and volume fraction (VF) in Cartesian meshes [22]. The volume fraction is defined as the ratio of the open volume to the total volume in a cell. The three area fractions (components of AF in x, y and z directions) are defined at the three cell faces in the increasing cell index directions as the ratio of the open area to the total area. This technique introduces the AF and VF into the conservation equations in order to include the effect of various geometries. At every time step, the area and volume fractions are calculated to describe the updated location of the object and its orientation in the fixed rectangular mesh [27]. In order to account for the fluid displacement due to the moving objects an additional source term is included in both the continuity equation and VOF transport equation. To include the effect of object boundaries, the tangential velocity of the object is introduced in the shear stress terms in the momentum equation.

The equations of motion of the rigid body are

$$\vec{F} = m\frac{d\vec{V}}{dt} \quad \text{and} \quad \vec{M} = [I]\frac{d\vec{\Omega}}{dt} + \vec{\Omega} \times ([I].\vec{\Omega}) \tag{1}$$

where $\vec{F}$ and $\vec{M}$ are the force and moment (about the mass center G of the body) vectors respectively, m is the mass of the body, $[I]$ is the moment of inertia tensor of the body and $\vec{V}$ and $\vec{\Omega}$ are the translational and rotational velocity vectors of the body, respectively. The velocity of a point on the surface of the body, $\vec{V}_B$, can be obtained from

$$\vec{V}_B = \vec{V} + \vec{\Omega} \times \vec{r} \tag{2}$$

where $\vec{r}$ is the vector from G to the point.

The continuity equation of fluid motion is

$$\frac{\partial \rho}{\partial t} + \nabla.(\rho \vec{u}) = S \tag{3}$$

where $\vec{u}$ is the fluid velocity vector, ρ is the fluid density and S is the mass source. In FAVOR method, the continuity equation can be interpreted as

$$\frac{\partial (\rho V_f)}{\partial t} + \nabla.(\rho \vec{u} A_f) = S_m \tag{4}$$

where V_f and A_f are the volume and area fractions respectively and S_m is the physical mass source term of the fluid. In case of moving objects (GMO), V_f and A_f vary with time and this effect on the fluid flow must be considered. Eq. (4) can be written as

$$\frac{V_f}{\rho}\frac{\partial \rho}{\partial t} + \frac{1}{\rho}\nabla.(\rho \vec{u} A_f) = -\frac{\partial V_f}{\partial t} + \frac{S_m}{\rho} \tag{5}$$

Comparing the above with Eq. (3) shows that the term $-\partial V_f / \partial t$ is equivalent to an additional volume source. In finite volume method of discretization, this source term exists only in mesh cells around the boundary of the moving object. In the water entry problem, there is no physical mass source and therefore $S_m = 0$. Also, the fluid can be considered incompressible and therefore $\partial \rho / \partial t = 0$. As a result, Eq. (5) reduces to

$$\nabla.(\vec{u} A_f) = -\frac{\partial V_f}{\partial t} \tag{6}$$

Wei [27] gave a new approximation for the volume source term due to the presence of the moving object as

$$\frac{\partial V_f}{\partial t} = \frac{S_B}{V_c}\vec{V}_B.\vec{n} \tag{7}$$

where, S_B is the surface area of the finite volume cell of the mesh on the boundary of the GMO in contact with the fluid, V_c is the volume of the finite volume cell of the mesh, $\vec{V}_B$ (see Eq. 2) is at the cell and $\vec{n}$ is the unit normal vector of the surface of the GMO at the cell.

Substitution of Eq. (7) in Eq. (6) gives

$$\nabla.(\vec{u} A_f) = -\frac{S_B}{V_c}\vec{V}_B.\vec{n} \tag{8}$$

which is the continuity equation that is solved in the present approach to the water entry problem.

The momentum equation is

$$\frac{\partial \vec{u}}{\partial t} + \frac{1}{V_f}(\vec{u} A_f).\nabla \vec{u} = \vec{X} - \frac{1}{\rho}\nabla p - \frac{1}{\rho}\nabla.(\tau A_f) \tag{9}$$

where p is pressure, τ is the viscous stress tensor and $\vec{X}$ is the body force vector.

The transport equation for VOF function F (fluid fraction) is

$$\frac{\partial F}{\partial t} + \frac{1}{V_f}\nabla.(F\vec{u}A_f) = -\frac{F}{V_f}\frac{\partial V_f}{\partial t} \tag{10}$$

Since in the water entry problem, the simulation adopts an 'incompressible flow with sharp interface' option where the object is dropped from 'void' under gravity to touchdown on the water surface , $F=1$ represents region occupied by the water and $F=0$ represents 'void' region, i.e. no fluid is present in that region.

During simulation, the equations of motion of the rigid body given in Eq. (1) are solved at each time step. The position, orientation and the area of volume fractions of the body (i.e. GMO) are calculated. The continuity equation, momentum equation and the VOF transport Eqs. (8)–(10) are solved numerically.

3. Model, computational domain and solver parameters

3.1. Model description

A rigid sphere of radius $R=0.15$ m and two rigid cones of radius $R=0.15$ m, but with different deadrise angles β (=45° and 20°) are chosen for the present study. Schematic diagrams of the models are shown in Fig. 1. The mass of the sphere, cone with $\beta=45°$ and cone with $\beta=20°$ are 11.5 kg, 10.2 kg and 9.8 kg, respectively, same as that of the models used in the experiments by De Backer et al. [7]. The vertical center of gravity (CG) of the sphere is 0.072 m below its center. In other words, the sphere is bottom heavy. The mass moments of inertia of the sphere in all three directions are $I_{xx}=I_{yy}=0.0687$ kg m^2 and $I_{zz}=0.0701$ kg m^2.

Simulations were performed for various touchdown velocities (V_0) The pressures are monitored at two locations designated P1 and P2 in Fig. 1. The pressure is expressed in terms of the pressure coefficient, C_p, defined as

$$C_p = \frac{P - P_\infty}{\frac{1}{2}\rho V_0^2} \tag{11}$$

where P is the pressure, P_∞ is the atmospheric pressure (=101,325 N/m^2) and ρ is the density of water (=1000 kg/m^3).

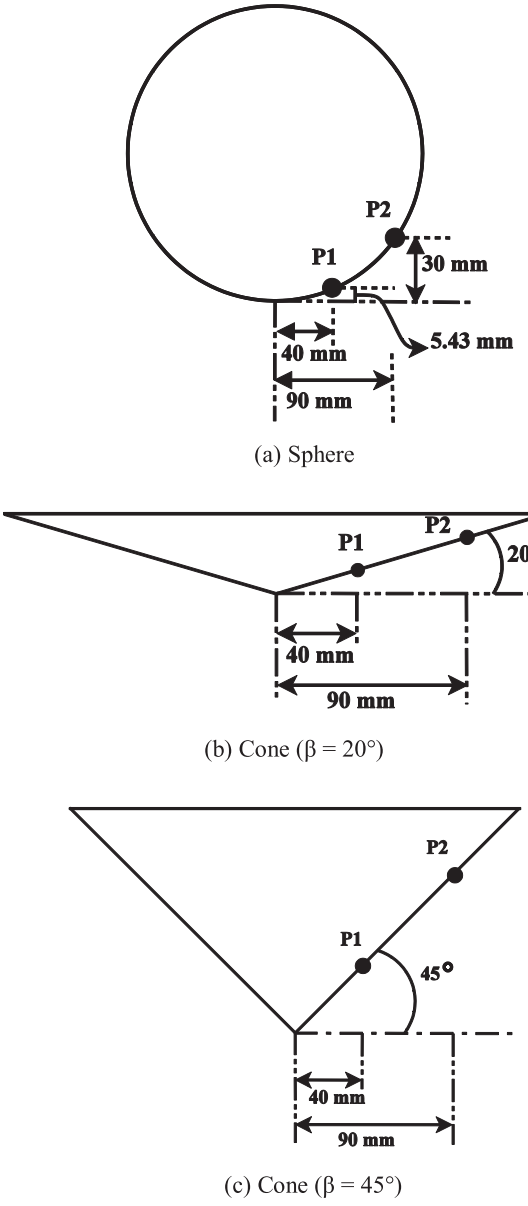

Fig. 1. Schematic diagram of the models and the locations of monitoring points P1 and P2.

3.2. Domain description

Two computational domains were used in the present study, one for estimating the maximum penetration depth and subsequent oscillations of the buoyant sphere (called full domain or Domain 1); and the other for the initial stage of water entry of both the sphere and cones to validate with the experiments (called half domain or Domain 2). The penetration depth (S) is the Z location of the bottom most point of the body below the undisturbed free surface $Z=0$ and is measured positive downwards from this free surface. The full domain replicates the rectangular tank used in the experiments and is same as the dimensions of this tank, namely, 1.2 m × 1.0 m × 2.7 m in x, y and z directions, respectively and is shown in Fig. 2(a). The half domain utilizes the symmetry of the problem and models one half of the full domain with half of the falling object in order to reduce the computational time and its size is 0.6 m × 1 m × 1 m and is shown in Fig. 2(b).

The Domain 1 was discretized uniformly with hexahedral elements and the element edge length being 10 mm. It consisted of 3.24 million cells and a computational time of 21 h 56 min was required for a simulation time of 10 s using a Windows based computer with i7 processor having 4 cores and a speed of 3.2 GHz and 16 GB RAM.

The Domain 2 uses a smaller mesh size which is essential to capture the impact pressure. It is impractical to uniformly discretize the entire domain with very small

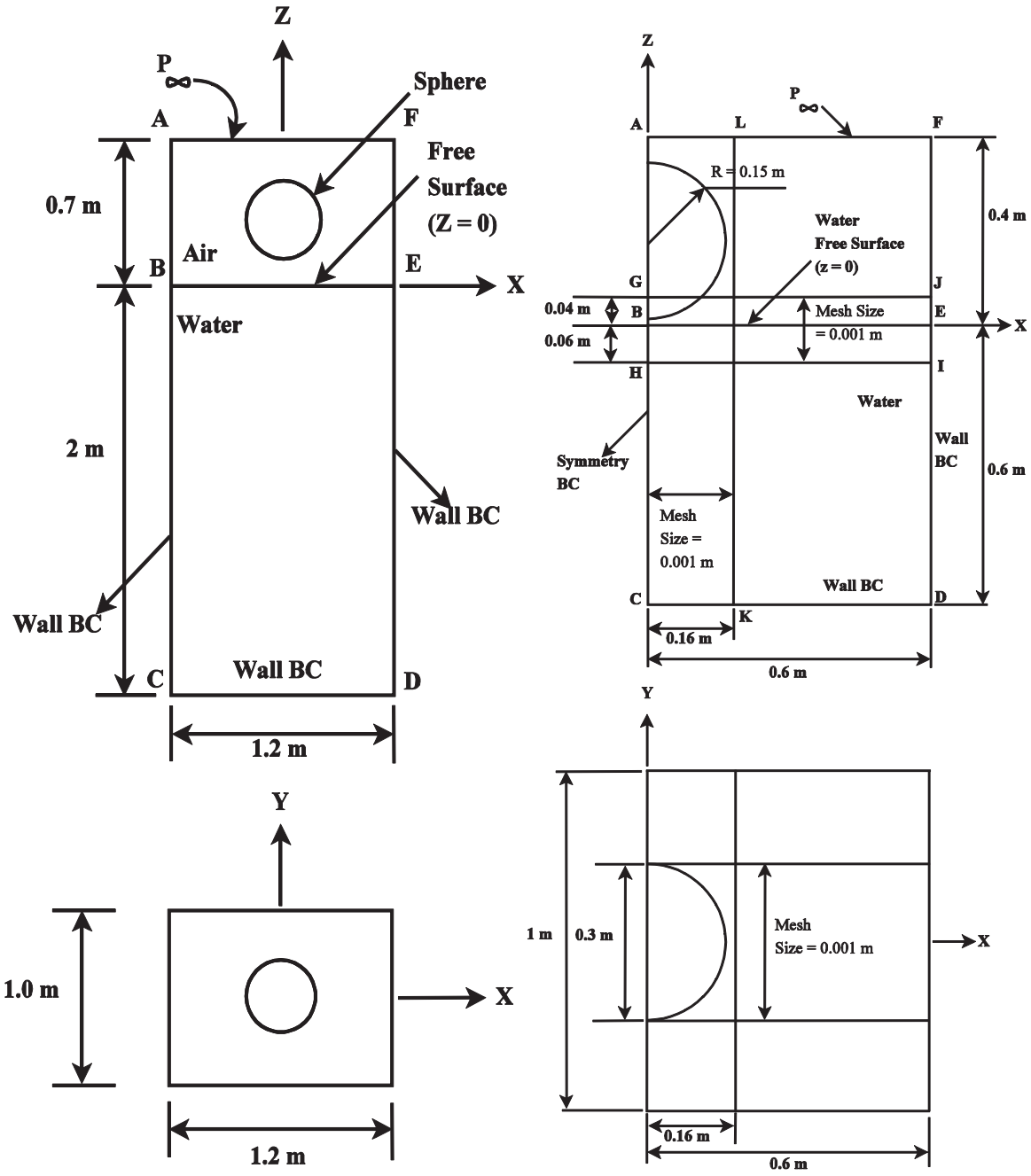

(a) Domain 1 (Full Domain) (b) Domain 2 (Half domain)

Fig. 2. The computational domains and the coordinate system.

mesh size. Hence an interaction region was identified, which consists of the combination of the region GHIJ measuring $0.6\,\text{m} \times 1\,\text{m} \times 0.1\,\text{m}$ and the region ALKC measuring $0.16\,\text{m} \times 1\,\text{m} \times 1\,\text{m}$ as shown in Fig. 2(b), to capture the impact phenomenon accurately. The interaction region consists of uniformly discretized hexahedral cells with edge length of 1 mm in all three directions. Coarser mesh size was used for other regions by choosing a suitable grading of mesh size (a growth ratio of about 1.1) so that at the boundaries the edge length of elements was about 25 mm. The mesh is shown in Fig. 3. The number of cells in this mesh was 10.1 million. In this figure, the interaction region, due to its very high mesh density, seems painted black.

The domain for the water entry problem is modeled as partly air and the rest water, with the sphere initially in the air and then moving under the influence of gravity and entering the water with a specific touchdown velocity. Since the water entry phenomenon is generally not affected by the presence of air, the air domain is modeled as a vacuum. This reduces the problem from two-fluid problem to one fluid prob-

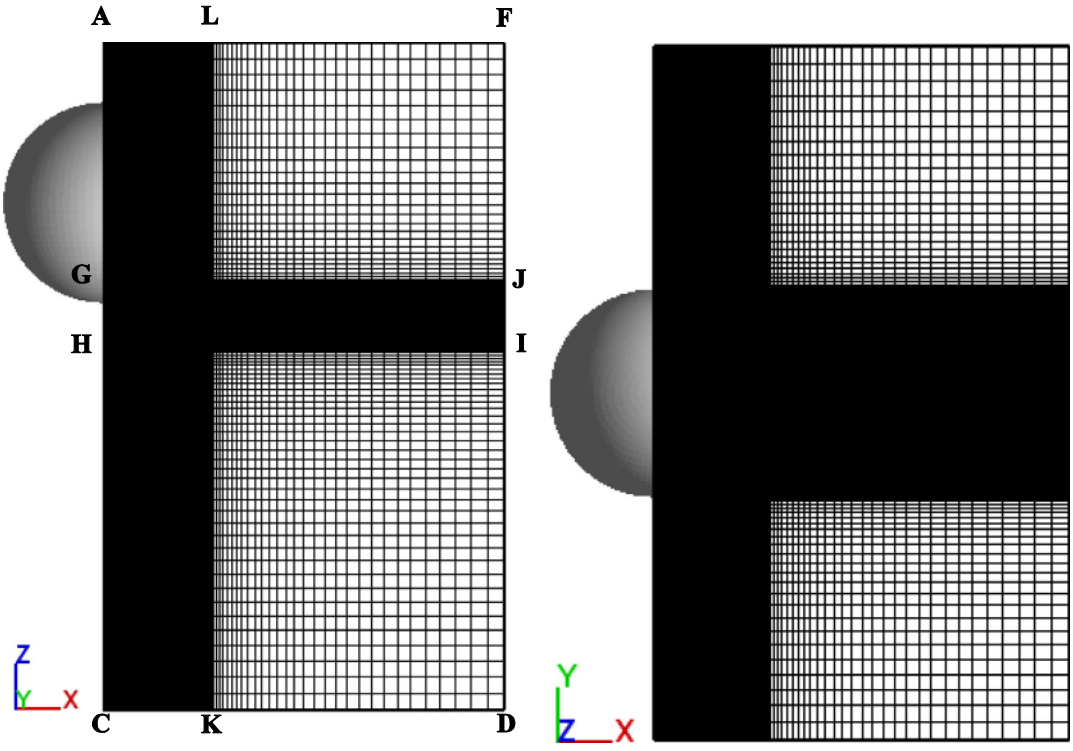

a) Front View b) Top View

Fig. 3. Mesh of Domain 2.

lem with sharp interface and it greatly helps in reducing the computation time.

The boundary conditions (BC) were assigned to numerically resemble the boundary conditions in the experiments. For both the Domain 1 and Domain 2, the top boundary (AF in Fig. 2) was assigned 'Specified Pressure' BC with a value of 101,325 N/m^2 ($=P_\infty$) in order to account for the atmospheric pressure. For the Domain 1, all the boundaries AC, CD and DF were assigned 'Wall' BC in order to resemble the tank walls. For the Domain 2, the boundary conditions are specified as 'Symmetry' in the symmetry plane (AC in Fig. 2(b) in XZ plane), 'Wall' boundary condition is specified on all other boundaries. The fluid was assumed to be incompressible. For the Domain 1, the flow was assumed turbulent (with k-ω SST model) since it is aimed to capture the full penetration depth and subsequent vertical oscillations where viscous forces are expected to be significant. For the Domain 2, the flow can be assumed inviscid since this model is used to capture early time behavior where viscous forces are expected to be insignificant compared to the inertial and impact forces. For the Domain 1, all degrees of freedom were allowed. For the Domain 2, only the vertical (or Z) translational degree of freedom was allowed in order to mimic the experimental condition of controlled water entry.

The height of the interaction region (BH in Fig. 2(b)) can be chosen based on the estimate of expected penetration depth. In this region, the impact (i.e. inertia) effect dominates, and therefore a larger height of this region is required for higher touchdown velocity so as to capture the transient pressure on the body accurately. The penetration depth data from the experimental studies were used for determining the height of the interaction region.

3.3. Solver parameters

The touchdown velocity (V_0) is defined as the velocity with which the body touches the air-water interface. All the models were kept at a distance of 0.01 m above the free surface of water and were given an initial velocity such that it achieved the desired touchdown velocity when acted upon by gravity ($g=9.81$ m/s^2). For example, an initial velocity of 3.9754 m/s was given to achieve a touchdown velocity of 4 m/s.

The data at the monitoring points (P1 and P2 in Fig. 1) were stored at each time step. The nominal time step used in the simulation was 20 μs (1 μs $=1\times10^{-6}$ s). The pressure is solved by the implicit solver using the iterative Generalized Minimum Residual (GMRES) method. The VOF advection scheme is specified with the option 'one fluid-sharp interface' [9].

4. Convergence study

The mesh convergence study was carried out using four mesh sizes for the Domain 2 for the sphere. The computed results are compared with experimental results of De Backer et al. [7]. The hexahedral mesh sizes in the interaction region (see Figs. 2 and 3) used were of edge length of 10 mm, 5 mm, 2.25 mm and 1 mm. The mesh of 1 mm edge length is

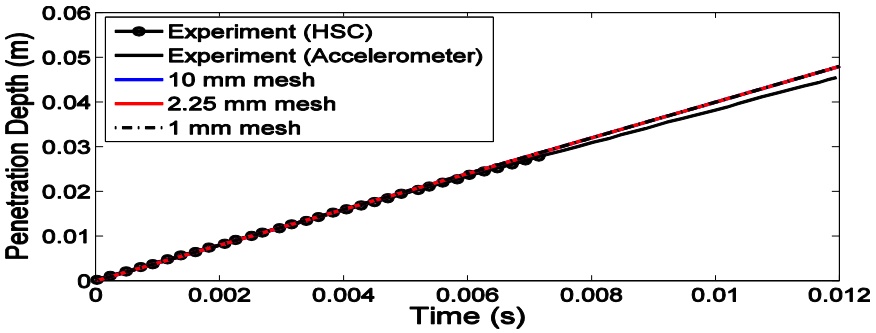

(a) Penetration depth variation with time

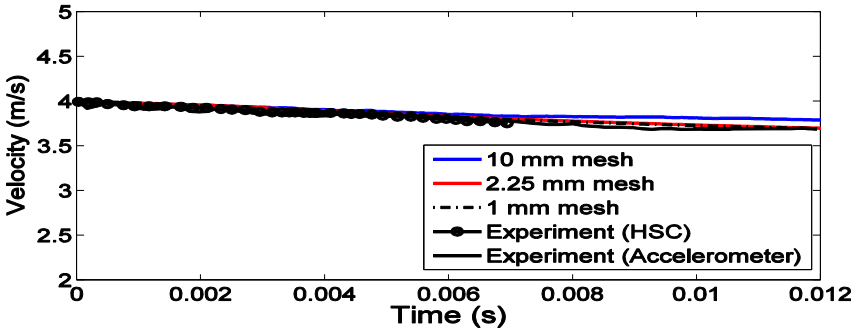

(b) Velocity variation with time

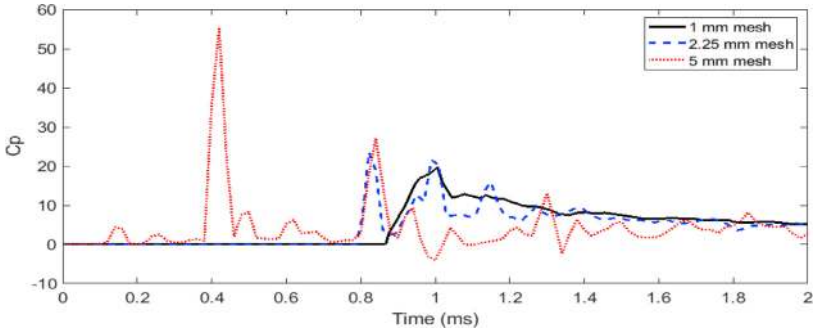

(c) Pressure variation with time at P1

Fig. 4. Mesh convergence study for the sphere ($V_0 = 4$ m/s) with time step of 20 μs.

shown in Fig. 3. The number of cells for these four mesh sizes were about 0.17 million for 10 mm, 0.51 million for 5 mm, 2.03 million for 2.25 mm and 10.19 million for 1 mm edge length. For a touchdown velocity of 4 m/s, the penetration depth (S) and velocity (v) as functions of time are plotted in Fig. 4(a) and (b), respectively, for mesh sizes 10 mm, 2.25 mm and 1 mm. The penetration depth variation is almost identical for all three mesh sizes. The velocity variation is almost identical for mesh sizes 2.5 mm and 1 mm (and also for mesh size 5 mm, though not plotted) and compare well with the experimental result, but is only slightly different for mesh size 10 mm.

The variation of pressure at the location P1 with time is plotted in Fig. 4(c) for mesh sizes 5 mm, 2.25 mm and 1 mm. The results, especially for the peak pressure, are widely different for these three meshes and it will be shown later that the result by the mesh size 1 mm matches best with the experimental result.

The main conclusion of this mesh convergence study is significant. It establishes that whereas a coarse mesh is satisfactory for prediction of velocity and hence the penetration depth, but a fine mesh is required for acceptable prediction of peak pressure on impact.

The accuracy of the solution also depends on the appropriate choice of the time step in the simulation. The solver uses an adaptive time stepping scheme wherein a nominal time step is input by the user. The solver adjusts this time step, if needed, in accordance with the physics of the problem to keep the simulation in the numerically stable range so that convergence is assured. In Fig. 5(a), the variation of the adaptive time steps is plotted as a function of time for two values of the nominal time step, 20 μs and 10 μs for the

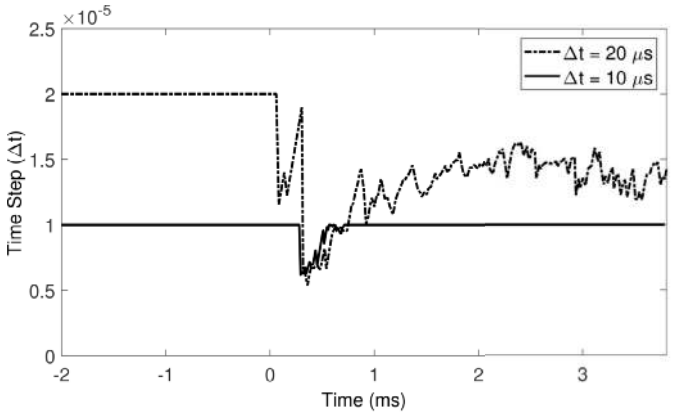

(a) Adaptive time step variation with time for the sphere

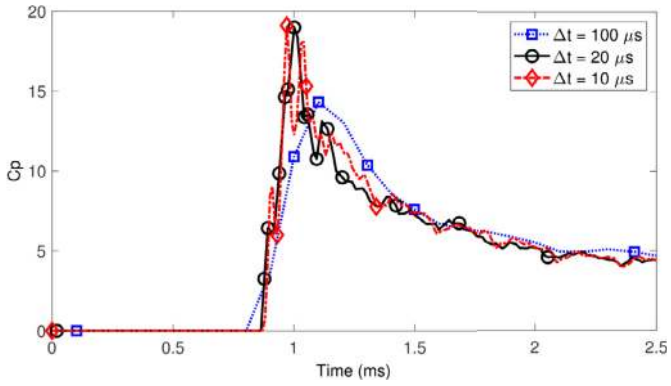

(b) Pressure variation with time

Fig. 5. Time step convergence study for the sphere ($V_0 = 4$ m/s) with 1 mm mesh size.

sphere with touchdown velocity of 4 m/s. The pressure variation at P1 for these two nominal time steps as well as for a nominal time step of 0.1 ms (1 ms = 1×10^{-3} s) are shown in Fig. 5(b).

From these two plots it is seen that the nominal time step is the upper bound of the adaptive time step. The peak pressure (given by C_p) predicted are $C_p = 18.98$ and 19.11 for the nominal time steps of 20 μs and 10 μs, respectively, and $C_p = 14.32$ for the nominal time step of 0.1 ms, the experimental value being $C_p = 18.9$. Clearly, the nominal time steps of 20 μs and 10 μs predict the peak pressure accurately and therefore a nominal time step of 20 μs has been chosen in all calculations. Fig. 5(a) indicates that a time step value of about 15 μs will suffice to capture the pressures beyond the peak pressure. However, around the time when the peak pressure occurs, the adaptive algorithm of the solver uses time step values as low as 6 μs. It is therefore clear that the adaptive algorithm plays an important role to substantially reduce the computational time required for simulation.

Finally, it should be pointed out that all pressure time histories in all calculations presented in this paper have been obtained by filtering the CFD results using a FIR filter wherein all frequencies above 10 Hz are removed and data is smoothed by a moving average technique, namely, a robust local regression using weighted linear least squares technique, subsequently.

5. Results and discussion

5.1. Sphere: validation with experiments

The CFD results for the sphere and their comparison with experimental results of De Backer et al. [7] wherever possible are presented in Fig. 6. The mesh, nominal time step, simulation time and computation time are given in Table 1.

The comparison of the velocity variation with penetration depth is shown in Fig. 6(a) for three touchdown velocities, namely, $V_0 = 2.88$ m/s, 4 m/s and 5 m/s, all showing very accurate match. The comparison of the penetration depth variation with time is shown in Fig. 6(b) for a touchdown velocity of $V_0 = 4$ m/s showing similar match. The comparison of the velocity variation with time is shown in Fig. 6(c) for a touchdown velocity of $V_0 = 4$ m/s, showing accurate match. The time variation of the total hydrodynamic force on the sphere, as obtained from CFD simulation, is shown in Fig. 6(d). It may be noted that at 10 ms, the maximum time in Fig. 6(d), the penetration depth of the sphere is only about 0.037 m as shown in Fig. 6(b). At this draft, the hydrostatic (i.e. buoyancy) force on the sphere is only about 5.8 N. This value is too small in comparison to the total vertical force of 425 N, showing the overwhelming contribution of hydrodynamic impact to the vertical force in comparison to the hydrostatic force. The comparison of the pressure (given by C_p) variation with time is shown in Fig. 6(e) for a touchdown velocity of $V_0 = 4$ m/s at locations P1 and P2 showing accurate match at the location P1 which registered peak measured pressure in the experiments, but somewhat poorer match (abou t 18% difference) at the location P2. The time instance of the peak pressure at P1 (about 0.001 s after touchdown) is also accurately captured in the simulation. The maximum C_p and the time instant at which it occurs are summarized in Table 2 at locations P1 and P2 and compared with experimental as well as FEM computed values from the literature.

For three touchdown velocities, the CFD results for the penetration depth, velocity, acceleration and pressure, all as functions of time, are presented in Fig. 7. Pre-touchdown acceleration is simply $g = 9.81$ m/s^2. On touchdown, the body with higher touchdown velocity will lose more acceleration as is evident from Fig. 7(c). The variation of the maximum values of C_p as function of V_0 can be obtained from Fig. 7(d). Based on only three data points of Fig. 7(d), this variation is almost linear. However, more numerical exercise is required to obtain the actual variation over a wider range of touchdown velocities.

The time sequence of images obtained during the simulation is shown in Fig. 8 and these are compared with the images captured by the high speed camera during the experiments. The qualitative comparison of the penetration depth shows good agreement between the experimental and CFD images. The water surface is observed to rise along the surface in both, but with the difference that in the experiments

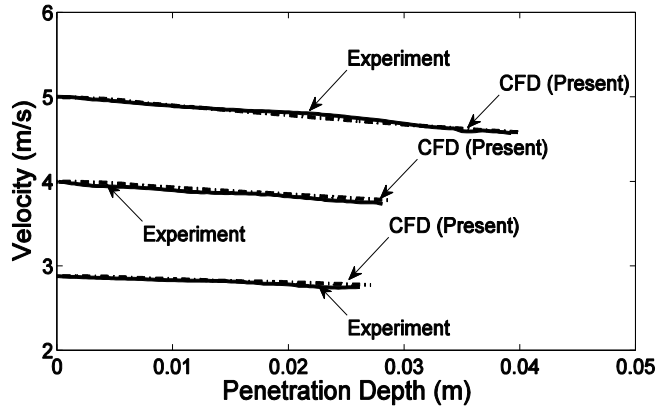

(a) Velocity variation with penetration depth (V_0 = 5 m/s, 4 m/s and 2.88 m/s)

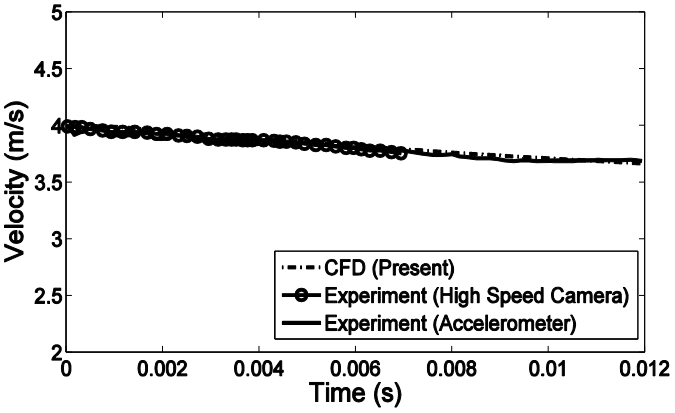

(c) Velocity variation with time (V_0 = 4 m/s)

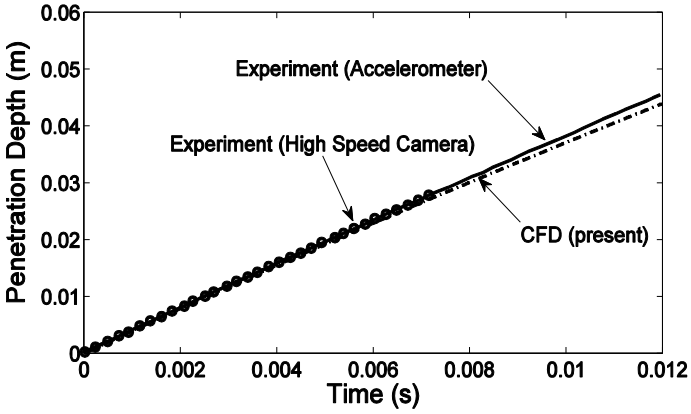

(b) Penetration depth variation with time (V_0 = 4 m/s)

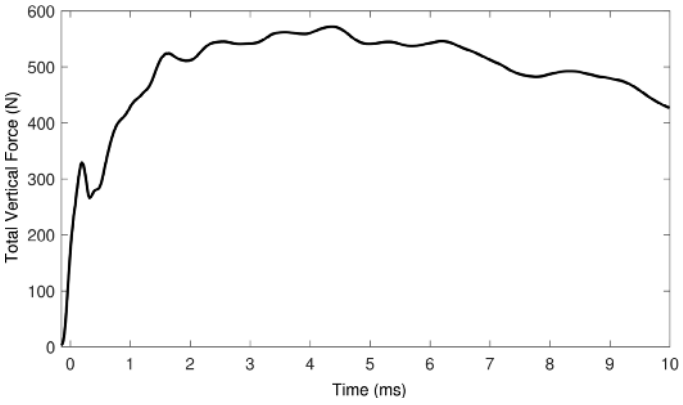

(d) CFD result for variation of total vertical force with time (V_0 = 4 m/s)

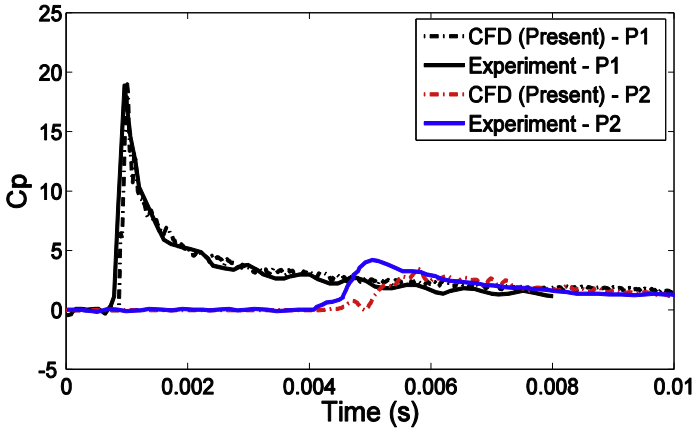

(e) Variation of pressure coefficient with time (V_0 = 4 m/s)

Fig. 6. The comparisons of CFD results with experiments for the sphere.

the water surface detached from the sphere and ends up forming a spray which could not be captured in CFD simulation.

5.2. Cones: validation with experiments

The comparisons of CFD results with experimental results of De bacler et al. [7] for the cones are presented in Fig. 9 for 20° deadrise angle and in Fig. 10 for 45° deadrise angle. The mesh, nominal time step, simulation time and computation time are given in Table 1. The comparison of the velocity variation with penetration depth is shown in Fig. 9(a) for three touchdown velocities, namely, $V_0 = 2.76$ m/s, 3.85 m/s and 4.67 m/s, for the 20° cone, all showing good match. The same quality of comparison is found in Fig. 10(a) for the 45° cone for three touchdown velocities, namely, $V_0 = 2.88$ m/s, 4.05 m/s and 4.9 m/s.

Table 1
Key parameters of the CFD set up for Domain 2.

	Sphere	20° cone	45° cone
Edge length of cells in the interaction region	1 mm	1 mm	1 mm
Nominal time step	20 μs	20 μs	10 μs
Z-extent of the interaction region	0.1 m	0.085 m	0.13 m
Simulation time	0.012 s	0.012 s	0.03 s
Computation time	17 h	13.5 h	32.5 h
Courant number	0.08 ($V_0 = 4$ m/s)	0.077 ($V_0 = 3.85$ m/s)	0.04 ($V_0 = 4.05$ m/s)
Circumferential mesh density at $R = 0.09$ m (P2) (No. of cells per degree)	1.6	1.6	1.6

($1\,\text{ms} = 1 \times 10^{-3}$ s; $1\ \mu\text{s} = 1 \times 10^{-6}$ s).

Table 2
Comparison of CFD results with experiments and FEM results.

Method	Sphere		20° cone		45° cone	
	P1 Max C_p (time in s)	P2 Max C_p (time in s)	P1 Max C_p (time in s)	P2 Max C_p (time in s)	P1 Max C_p (time in s)	P2 Max C_p (time in s)
Experiment [7]	18.89 (0.00096)	4.21 (0.005)	8.356 (0.0032)	9.832 (0.0072)	2.218 (0.009)	1.21 (0.0195)
FEM [26]	16.46 (0.00093)	4.752 (0.005)	7.95 (0.00325)	10.13 (0.0069)	1.358 (0.009)	1.56 (0.021)
CFD (Present)	18.98 (0.001)	3.45 (0.0057)	8.14 (0.0032)	9.62 (0.0071)	1.94 (0.009)	1.615 (0.0208)

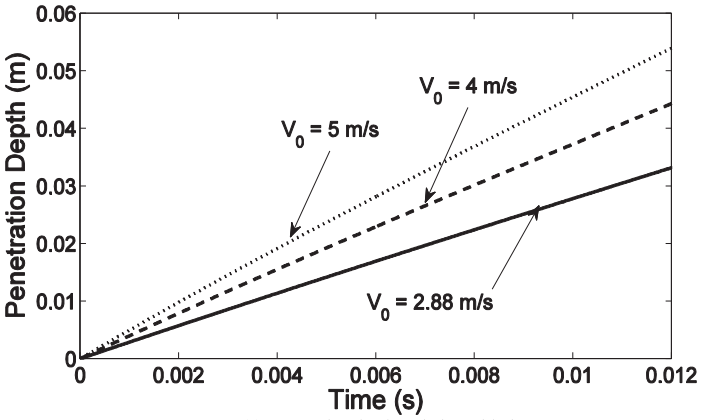

(a) Penetration depth variation with time

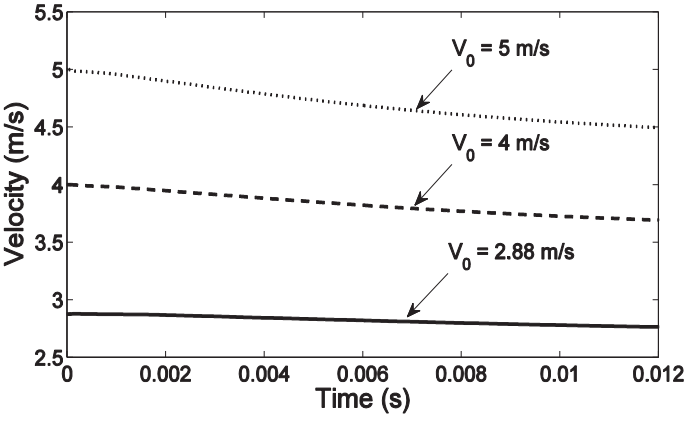

(b) Velocity variation with time

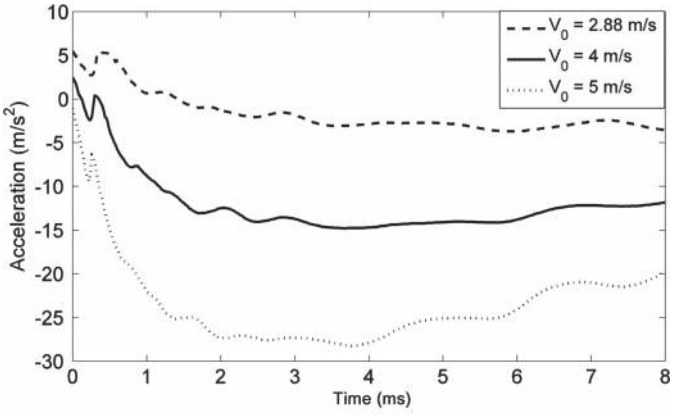

(c) Acceleration variation with time

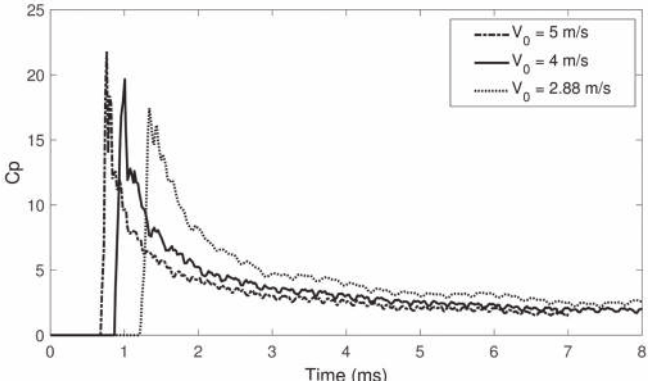

(d) Variation of pressure coefficient with time at P1 location

Fig. 7. CFD simulation results for the sphere.

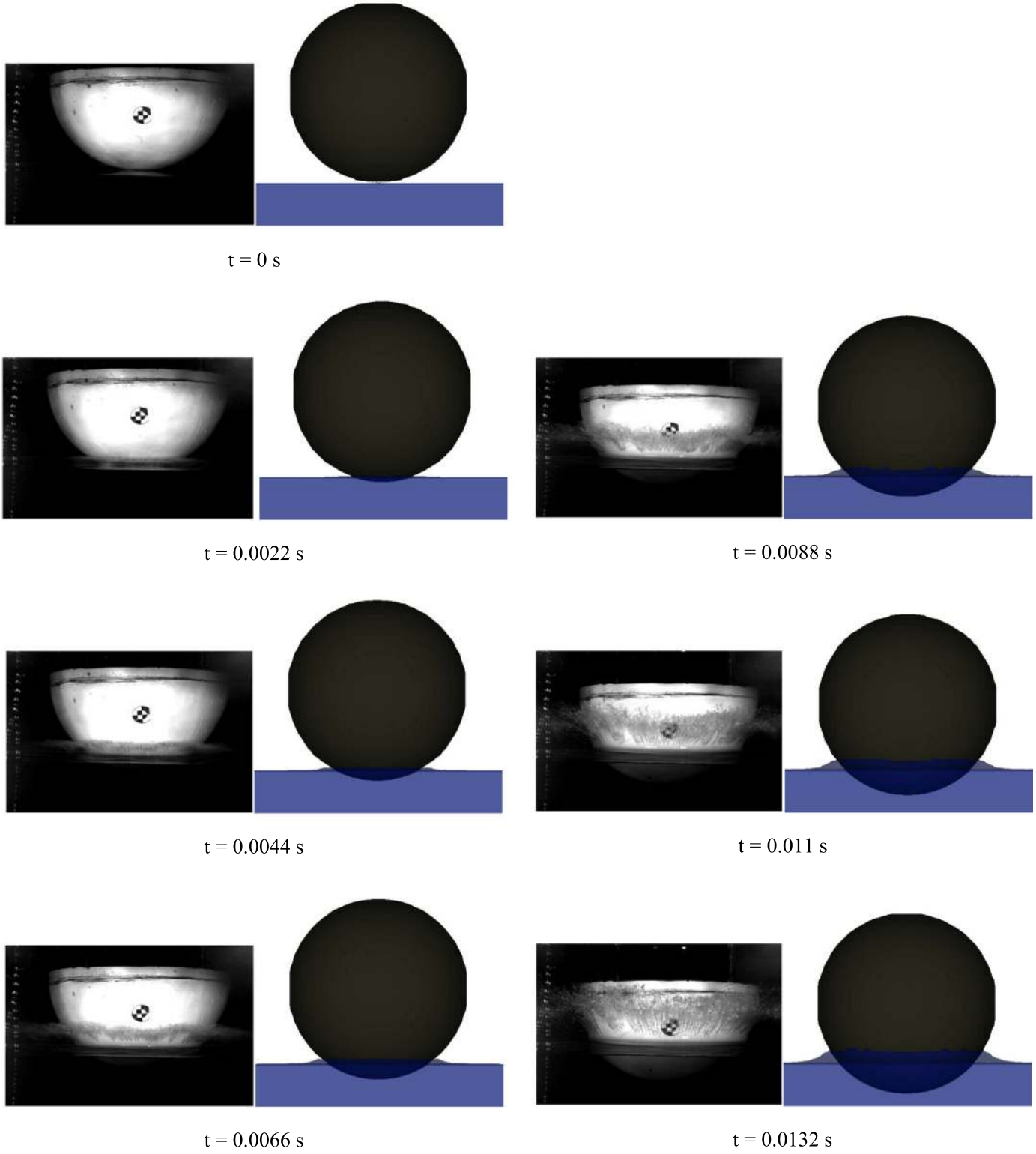

Fig. 8. Comparison of the experimental and simulation images of the sphere ($V_0 = 4$ m/s).

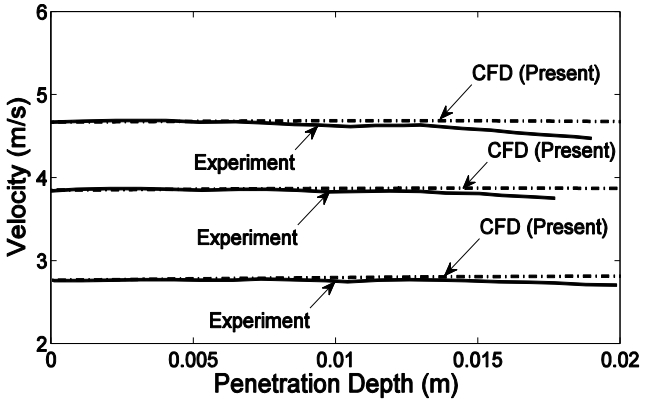

(a) Velocity variation with penetration depth (V_0 = 4.67 m/s, 3.85 m/s and 2.76 m/s)

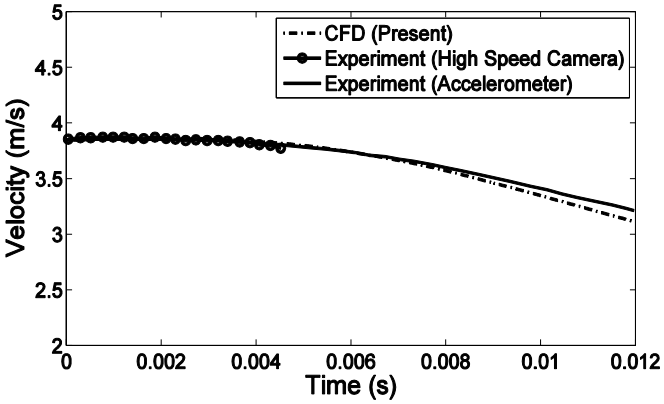

(c)Velocity variation with time (V_0 = 3.85 m/s)

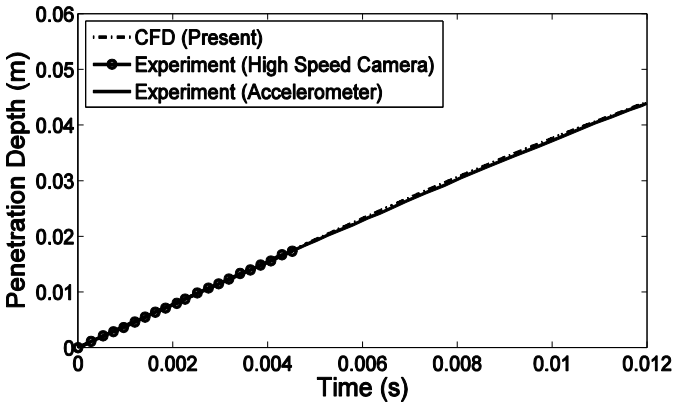

(b) Penetration depth variation with time (V_0 = 3.85 m/s)

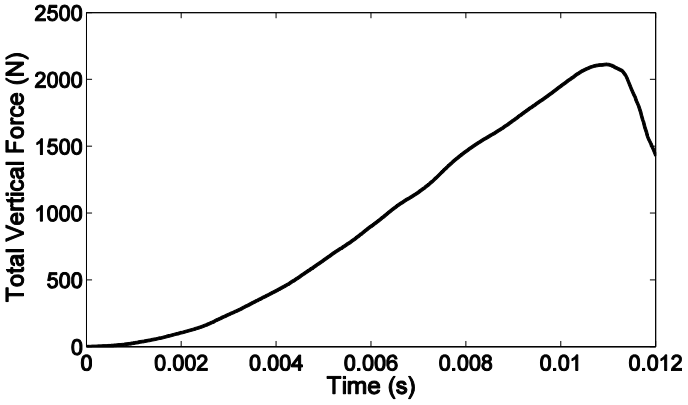

(d) CFD result for variation of total vertical force with time (V_0 = 3.85 m/s)

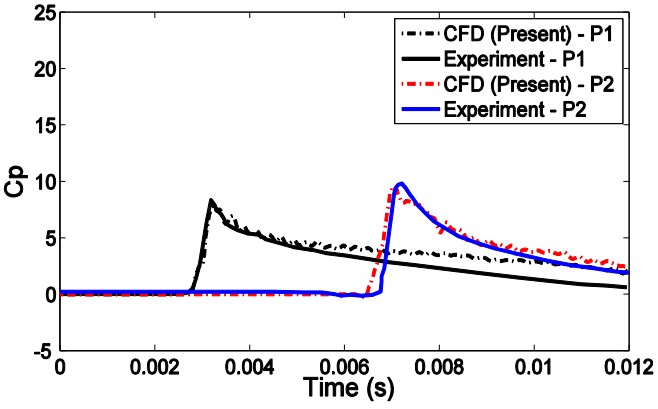

(e) Variation of pressure coefficient with time (V_0 = 3.85 m/s)

Fig. 9. The comparisons of CFD results with experiments for the cone ($\beta = 20°$).

The comparison of the penetration depth variation with time is shown in Fig. 9(b) for a touchdown velocity of $V_0 = 3.85$ m/s for the 20° cone and in Fig. 10(b) for a touchdown velocity of $V_0 = 4.05$ m/s for the 45° cone, both showing accurate match.

The comparison of the velocity variation with time is shown in Fig. 9(c) for a touchdown velocity of $V_0 = 3.85$ m/s for the 20° cone and in Fig. 10(c) for a touchdown velocity of $V_0 = 4.05$ m/s for the 45° cone, both showing accurate match. The time variations of the total hydrodynamic force on the two cones, as obtained from CFD simulation, are shown in Figs. 9(d) and 10(d).

The comparison of the pressure (given by C_p) variation at locations P1 and P2 with time is shown in Fig. 9(e) for a touchdown velocity of $V_0 = 3.85$ m/s for the 20° cone and in Fig. 10(e) for a touchdown velocity of $V_0 = 4.05$ m/s for the 45° cone. In both cases, the peak pressures at both P1 and P2 as well as their corresponding time instants match very well with experiments, but the attenuation of pressure beyond this time instant shows a poorer match, the CFD predicted atten-

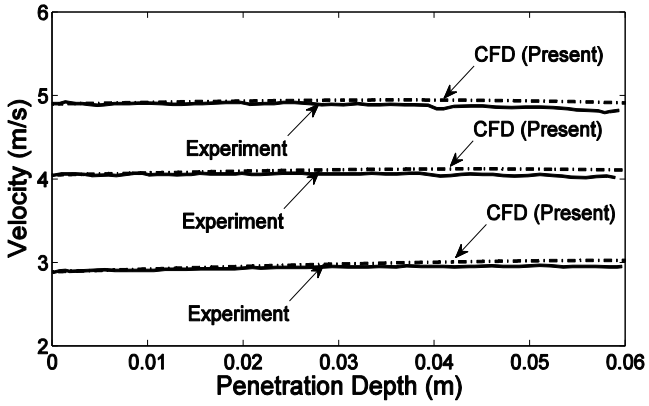

(a) Velocity variation with penetration depth (V_0 = 4.9 m/s, 4.05 m/s and 2.88 m/s)

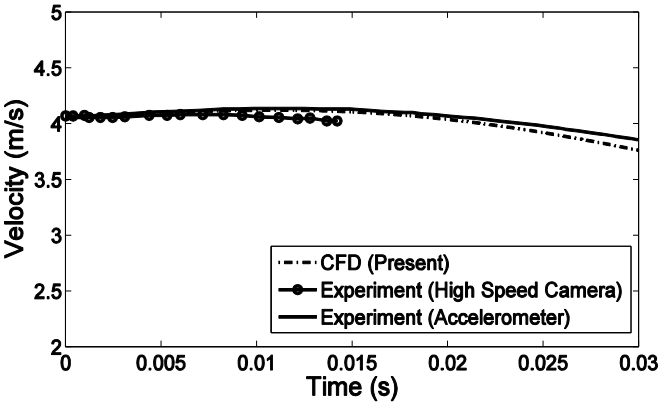

(c) Velocity variation with time (V_0 = 4.05 m/s)

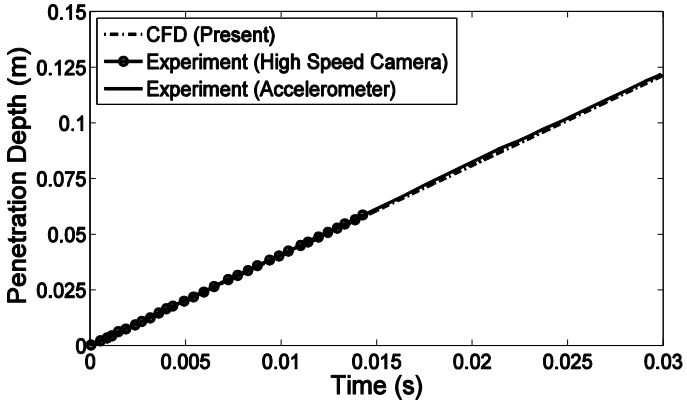

(b) Penetration depth variation with time (V_0 = 4.05 m/s)

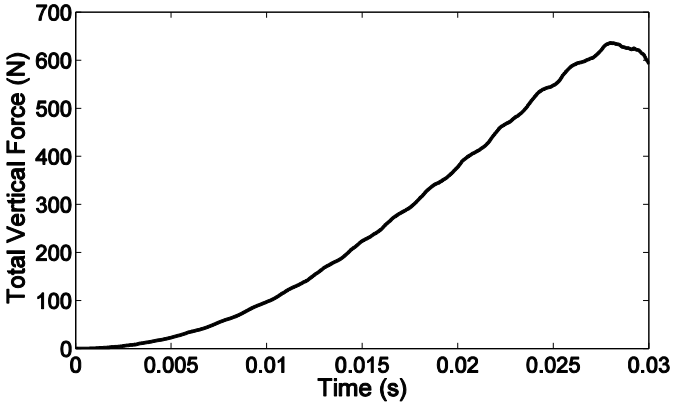

(d) CFD result for variation of total vertical force with time (V_0 = 4.05 m/s)

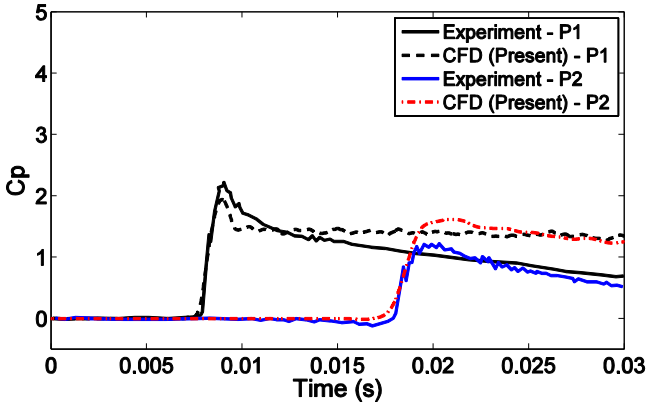

(e) Variation of pressure coefficient with time (V_0 = 4.05 m/s)

Fig. 10. The comparisons of CFD results with experiments for the cone ($\beta = 45°$).

uation being somewhat slower. Finally, the maximum C_p and the corresponding time instance are summarized in Table 2 and compared with experimental as well as FEM computed values from the literature.

5.3. Discussion on comparison of experiments for the sphere and cones

The detailed comparisons of CFD results with experiments of De Backer et al. [7] presented in Figs. 6, 8–10 and also a study of the numerical simulation results for the same experiments by Wang and Soares [26] by an explicit finite element method bring out the following:

(i) The penetration depth, vertical velocity and acceleration underwater can be accurately predicted with a wide range of mesh densities (1 mm–10 mm edge length). However, the impact pressure can only be predicted accurately by a 'very fine' mesh density (1 mm edge length). In order to achieve a practical size of the problem (i.e. number of cells), in the present work an

interaction region has been proposed close to the body where a 'very fine' mesh is used and other regions are modeled with a graded mesh starting from the boundaries of the interaction region.

(ii) From Table 2, it is seen that the peak pressure at the P1 location and the corresponding time instance are very well captured in the present CFD approach for all three bodies and the quality of comparison (i.e. with experiments) is superior to the FEM results. However, at the P2 location, the quality of peak pressure comparison by both CFD and FEM is poor (over 12% error) for the sphere; good for the 20° cone by both methods (under 5%), and poor for the 45° cone (about 30% error) by both CFD and FEM. The reason for this is not clear. Since both FEM and CFD yield large peak pressure error at the P2 location of the sphere, all other parameters being predicted accurately, it may have to do with the measurement inaccuracies contributed by the curvature of the sphere and its interaction with the deforming free surface.

(iii) The nominal time step used in CFD was 20 μs with adaptive time stepping capability. For the entire simulation the time step actually used was about 15 μs. This seems to be far larger than that reported in Wang and Soares [26], namely 0.114 μs. As a result, whereas Wang and Soares [26] reported a computational time of about 46 h for a mesh consisting of about 0.5 million cells, in the present work a computational time of about 17 h was required for a model consisting of about 10 million cells.

(iv) A computational time of about 17 h for about 10.19 million cells with fine mesh edge length of 1 mm recorded in the present work (in a PC with 3.2 GHz processor speed and 16 GB RAM) seems to be superior than that reported in Wang and Soares [26], namely about 46 h for about 0.5 million cells with fine mesh edge length of 2.5 mm (in a PC with 2.5 GHz processor speed and 3 GB RAM). However, this requires further verification.

(v) Despite the apparent success of the CFD simulations, the question of choosing the appropriate mesh size for accurate prediction of peak pressure requires further study before firm recommendations can be made. However, the adaptive time stepping and the mesh density in the interaction region seems to be crucial in reducing the computational time. To put this in perspective, it turns out that 1 mm edge length of a cell in the interaction region translates to 1.6 cells/degree at the P2 location for all three bodies (see Table 1), showing that in order to predict the peak pressure accurately at a point, the mesh around it must have a very high spatial resolution. Regarding the choice of the time step (Δt), the Courant number ($C = u\ \Delta x/\Delta t$) calculated on the basis of the touchdown velocity ($u = V_0$) and the cell length of 1 mm ($= \Delta x$) are listed in Table 1 for a few cases. The CFD code that had been used in the present work implements an explicit formulation for the solution of equations and hence the Courant number (which should be less than unity) is relevant. A value of $C \approx 0.05$ seems to be good for all simulations. However, this can be confirmed only if one has experimental results for the chosen body shapes at a larger scale.

6. Sphere: free oscillatory motion

The mass of the sphere is 11.5 kg and its buoyancy is 14.137 kg and therefore it is buoyant. In the experiments, the water entry was controlled to occur in Z-direction alone and most measurements were reported for about 0.012 s, a time in which the penetration depth was less than 50 mm, which is less than one sixth the diameter of the sphere ($= 300$ mm). Since the focus of the experiments was the impact phenomenon, the time was restricted to adequately cover the impact alone. In a free fall of the sphere in water without any restriction on either the direction of motion or on time, its buoyancy will ensure that it penetrates up to a maximum depth where the vertical velocity becomes zero and then the buoyant force will make it rebound till its upward velocity becomes zero. This will be followed again by a penetration (or entry) phase followed by a rebound (or exit) phase. These oscillations will continue till the time the sphere comes to rest. A rebound phase is essentially the 'water exit' problem. Beyond the 'early times' where impact is no longer relevant, the viscous forces become important in governing the motion of the sphere and hence a turbulent model needs to be adopted. As a result, the symmetry of the problem no longer exists and the sphere will not move in the Z-direction alone. It will have motions in X- and Y-directions due to the unsymmetric nature of the small hydrodynamic forces generated in these directions and zero stiffness in these directions. Also, depending on its stability, the sphere can also rotate.

In this section, this 'full' motion of the sphere is simulated in the same tank using uniform 10 mm mesh in Domain 1 (see Fig. 2 and Section 3.2) and the results are presented where the sphere motion is free in all degrees of freedom and the time of simulation is long enough (about 10 s) so that the sphere either 'almost' comes to rest after several cycles of penetration and rebound oscillations or touches the tank wall.

The simulations were performed with touchdown velocities $V_0 = 2.88$ m/s, 4 m/s and 5 m/s. Unlike the simulations reported in Sections 4 and 5, where only the Z degree of freedom (1-dof) of the body was allowed to mimic the experiments, for the present 'full' motion simulations, all 6 degrees of freedom (6-dof) of the sphere were allowed. The penetration depth variations with time are given in Fig. 11(a) and the velocity variations with time are given in Fig. 11(b). The maximum penetration depths for $V_0 = 2.88$ m/s, 4 m/s and 5 m/s are 1.21 m at $t = 1.109$ s, 1.55 m at $t = 1.195$ s and 1.81 m at $t = 1.136$ s, respectively. After reaching the maximum penetration depth (entry phase), the buoyancy makes the sphere to rebound (exit phase) till its velocity (vertical) becomes zero and then again due to its weight it penetrates again and this entry-exit cycle goes on till the sphere comes to rest. All the peaks of the penetration depth curve in Fig. 11(a) correspond

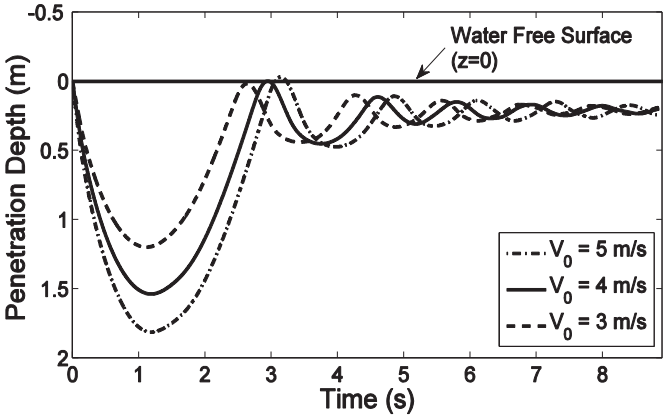

(a) Penetration depth variation with time

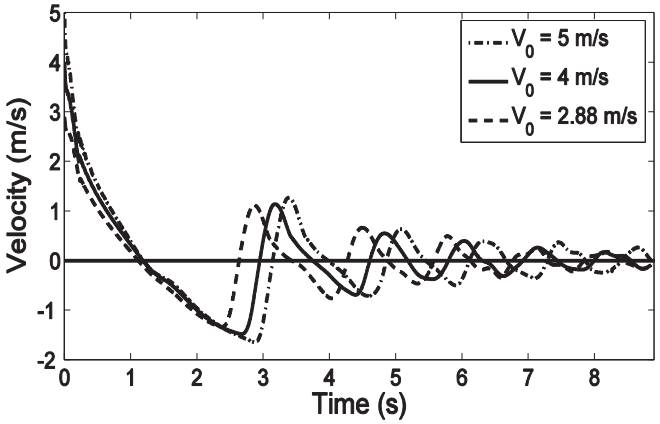

(b) Velocity variation with time

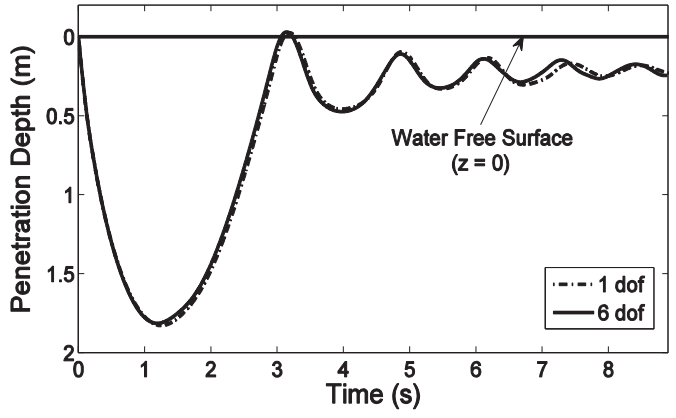

(c) Penetration depth variation with time for 1-dof and 6-dof models (V_0 = 5 m/s)

Fig. 11. Entry and exit oscillations of the sphere.

to zero vertical velocity in Fig. 11(b). Between two successive peaks of the penetration depth curve, the acceleration undergoes a change in sign. It can be seen from Fig. 11(a) that the small oscillations persist even at large time values in all cases.

In Fig. 11(c), the penetration depth variation with time for both 1-dof and 6-dof simulations are compared, showing excellent agreement. This is despite the fact that in the 6-dof simulation, the *X*- and *Y*-displacements occur as shown in Fig. 12, where the trajectories (*X–Z, Y–Z* and *X–Y* displacements) are shown for all three touchdown velocities. For $V_0 = 5$ m/s, the sphere collides in tank boundary during the rebound phase after a few oscillations, brought out by the fact that the trajectory (of the touchdown point of the sphere) touches $X = -0.45$ m (since the radius of the sphere is 0.15 m and the tank boundary is at $X = -0.6$ m).These trajectories represent the unstable behavior sensitive to the higher order (small) hydrodynamic forces that are computed by the CFD model. Though no experimental verification is available, actual trajectories will depend upon imperfection in model geometry, its hydrostatic stability, initial conditions and ambient disturbance. Therefore, it may be more challenging to obtain CFD validation of this behavior.

The main observations from these calculations are: (a) the 'full' motion of the sphere, of which the early time behavior is validated against experiments, combines the water entry and exit problems and can be handled by the CFD methodology that is adopted in the present work and (b) the behavior of the sphere beyond 'early time' shows unstable behavior in that the motion of the sphere has significant horizontal components of displacement due to three dimensional nature of the hydrodynamic force in the turbulent (viscous) flow regime.

7. Free surface deformation and its breaking

The fluid flow associated with the water entry problem involving the free surface is highly transient. Some of the CFD codes that can solve the Navier–Stokes equations are not equipped to include the free surface, which is a free boundary, in simulations. In a problem involving the free surface, the solution domain changes due to the movement of the surface and in turn, the surface motion is determined by the solution. The modification of the solution domain involves the changes in its size and shape, and in some cases may also involve the coalescence and break up of fluid regions which, in fact, is reflected as either loss and gain of the free surface. The VOF technique that has been used in the present work is ideally suited for the free surface tracking in the water entry problem, wherein the free surface is not directly defined, instead the location of the bulk fluid is defined. Because of this, the fluid regions can coalesce or break up and this does not translate to any computational difficulty.

The present CFD simulation predicts breaking of the free surface as brought out in Fig. 13 for the sphere and in Fig. 14 for the 45° cone. It may be seen that the time of first breaking is between $0.041\,\text{s} < t < 0.052\,\text{s}$ for the sphere with $V_0 = 4$ m/s. The experimental results for the sphere are available only up to $t = 0.012$ s and therefore up to this time breaking of the free surface does not occur. As a result, Fig. 13 has been obtained from continuing the same simulation (i.e. with the mesh of Fig. 3 which has densely meshed interaction region) up to 0.096 s. Fig. 14 shows that the time of first breaking is between $0.022\,\text{s} < t < 0.026\,\text{s}$ for the 45° cone with $V_0 = 4.05$ m/s and this time range is below 0.03 s up to which experimental results are available. It has been found that the free surface does not break for the 20° cone up to 0.012 s up to which experimental results are available and hence not shown.

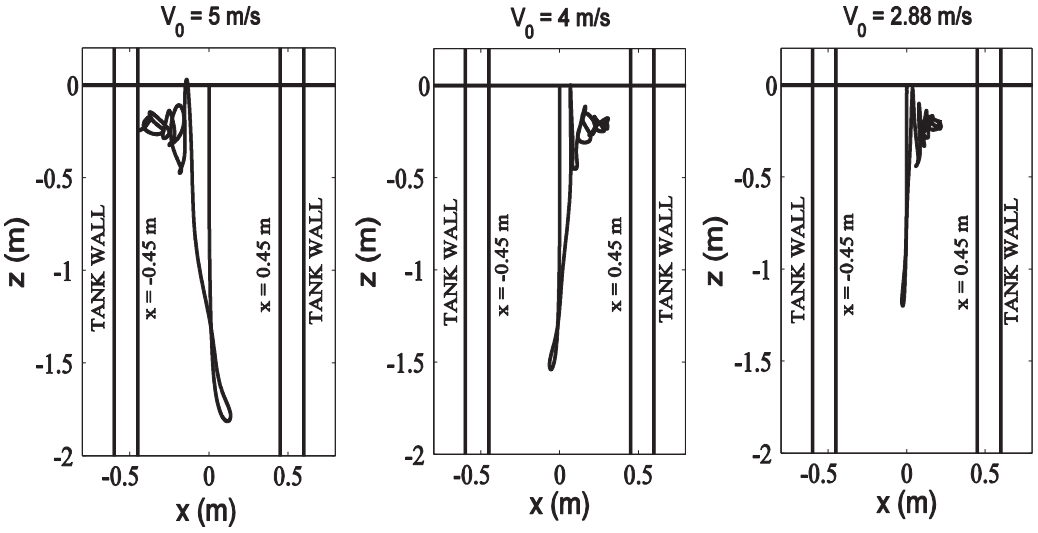

(a) Trajectory (displacement) in *x-z* plane

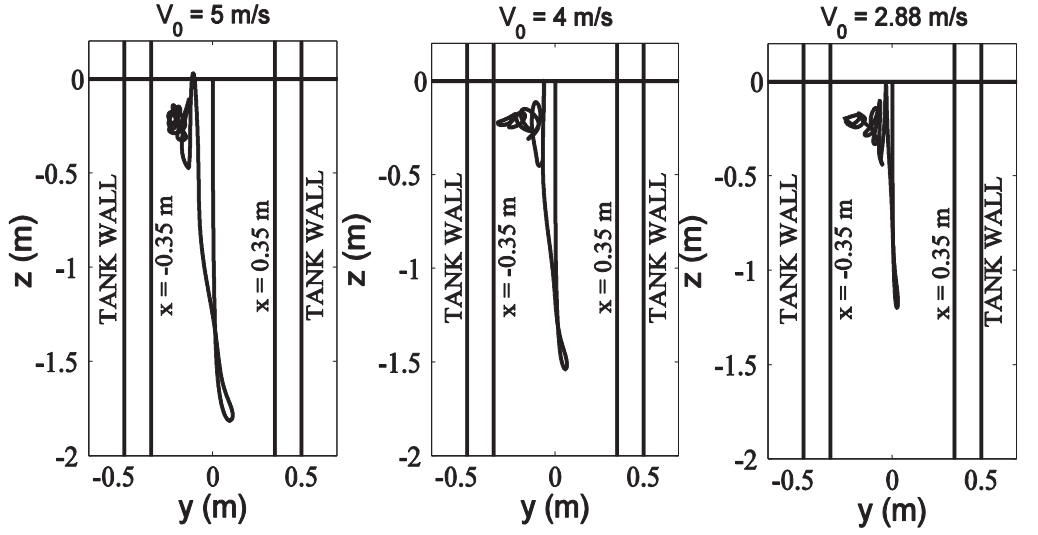

(b) Trajectory (displacement) in *y-z* plane

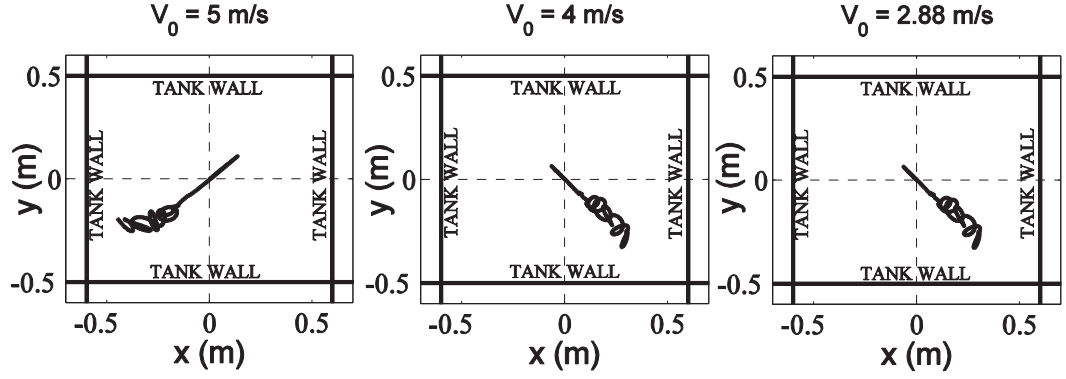

(c) Trajectory (displacement) in *x-y* plane

Fig. 12. Trajectories of the sphere covering entire entry and exit phases.

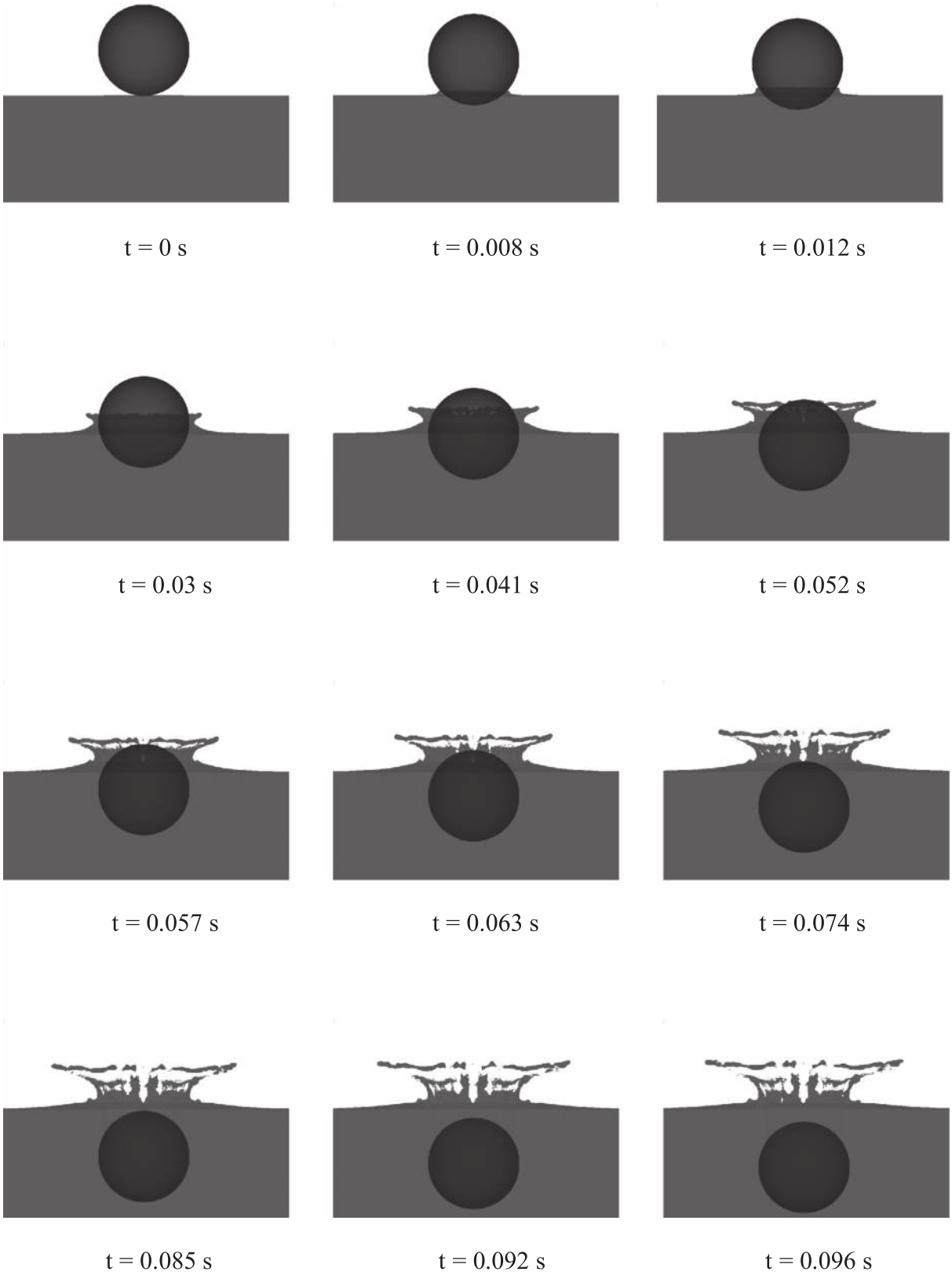

Fig. 13. Images of breaking of the free surface during water entry of a sphere at $V_0 = 4$ m/s.

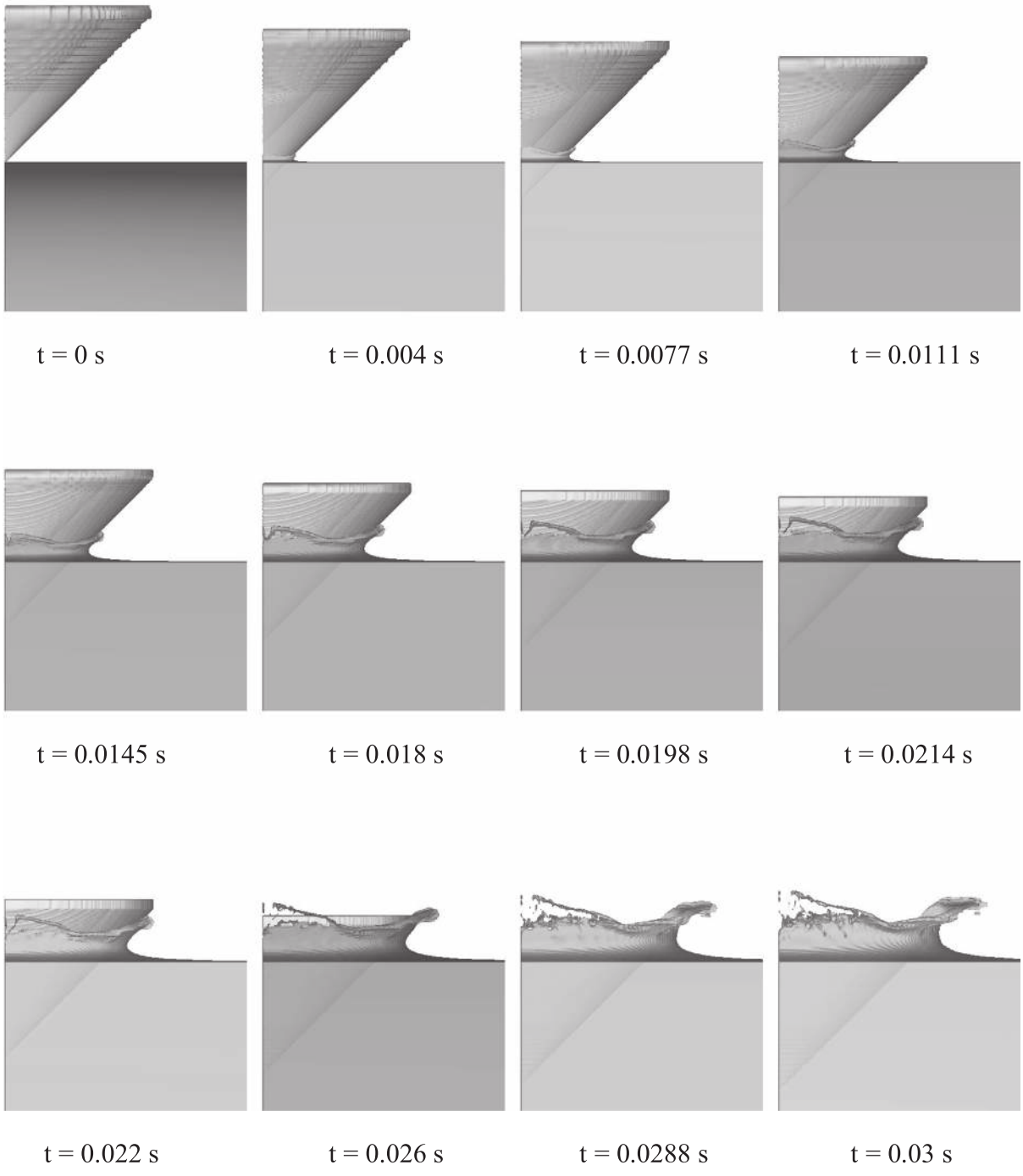

Fig. 14. Images of breaking of the free surface during water entry of 45° cone at $V_0 = 4.05$ m/s.

The main observation of this exercise is that to capture the breaking of the free surface, the fine mesh in the interaction region is required. The coarse mesh that has been used for the 'full' motion of the sphere cannot capture this with sufficient fidelity.

8. Conclusion

The results of the CFD simulation of water entry of a sphere and two cones at three touchdown velocities in the early phase are compared with recent experimental results and FEM results available in the literature. The main observation from this study is that whereas the penetration depth, velocity and acceleration can be predicted well with relatively coarse mesh with wide choice of spatial discretization, accurate prediction of the peak pressure on impact and prediction of breaking of the free surface require a much finer mesh in an interaction region around the trajectory of the body and appropriate choice of the time step with an adaptive time stepping strategy to reduce the computational effort. The results

obtained in this work show superior match with the experimental results at a much lower computational cost compared to recently published FEM results, especially in the prediction of the peak pressure.

The CFD simulation of the 'full' motion of the buoyant sphere, allowing 6-dof motion for several cycles of entry and exit phases, shows that the present approach can work equally well for both water entry as well as water exit problems. The CFD approach, which can model turbulence, is ideal for the combined entry-exit problem because the viscous forces become important after the initial impact. Also, the inherent three dimensional nature of turbulence destroys the symmetry of the trajectory and this expected behavior is correctly predicted by the present CFD simulation.

References

[1] S. Abrate, Appl. Mech. Rev. 64 (6) (2013) 1–35.
[2] A.E.M. Alaoui, A Nême, A Tassin, N. Jacques, Appl. Ocean Res. 37 (2012) 183–197.
[3] M.R. Alizadeh, A. Rabiee, M.M. Alishahi, in: Proceedings of the 13th Annual and 2nd International Fluid Dynamics Conference, Shiraz, Iran, 2010.
[4] N. Aquelet, M. Souli, L. Olovsson, Comput. Methods Appl. Mech. Eng. 195 (1–3) (2006) 110–132.
[5] J.L. Baldwin, Vertical Water Entry of Cones, Naval Ordinance Laboratory, Maryland, 1971 Technical Report 71-25.
[6] S.L. Chuang, D.T. Milne, Drop Tests of Cones to Investigate the Three--Dimensional Effects of Slamming, Naval Ship Research and Development Center, Washington, 1971 Report No. 3543.
[7] G. De Backer, M. Vantorre, C. Beels, J. De Pré, S. Victor, J. De Rouck, C. Blommaert, W. Van Paepegem, Appl. Ocean Res. 31 (3) (2009) 143–156.
[8] A.C. Fairlie-Clarke, T. Tveitnes, Ocean Eng. 35 (2008) 706–716.
[9] FLOW3D user manual (2013): Version 10.1, Flow Science Inc.
[10] K. Gong, H. Liu, B.L. Wang, J. Hydrodyn. Ser. B 21 (6) (2009) 750–757.
[11] M. Greenhow, Appl. Ocean Res. 9 (1987) 214–223.
[12] K.M.T. Kleefsman, G. Fekken, A.E.P. Veldman, B. Iwanowski, B. Buchner, J. Comput. Phys. 206 (2005) 363–393.
[13] A.A. Korobkin, V.V. Pukhnachov, Annu. Rev. Fluid Mech. 10 (1988) 159–185.
[14] P. Lin, Comput. Fluids 36 (2007) 549–561.
[15] A. May, J. Appl. Phys. 23 (1952) 1362–1372.
[16] T. Miloh, Appl. Ocean Res. 13 (1) (1991) 34–48.
[17] P. Maruzewski, D. Le Touze, G. Oger, F. Avellan, J. Hydraul. Res. 48 (2010) 126–134.
[18] C. Nisewanger, Experimental Determination of Pressure Distribution on a Sphere During Water Entry, NAVWEPS, 1961 Technical Report 7808.
[19] G. Oger, M. Doring, B. Alessandrini, P. Ferrant, J. Comput. Phys. 213 (2) (2006) 803–822.
[20] B. Peseux, L. Gornet, B. Donguy, J. Fluids Struct. 21 (3) (2005) 277–303.
[21] Z.R. Shen, D.C. Wan, in: Proceedings of the 21st International Offshore and Polar Engineering Conference, Maui, Hawaii, USA, 2011, pp. 695–702.
[22] J.M. Sicilian, (1990) A Favor Based Moving Obstacle Treatment for FLOW3D. Flow Science Technical Note #23 (FSI-90-TN23), Flow Science Inc.
[23] I. Stenius, A. Rosen, J. Kuttenleuler, Int. Shipbuild. Prog. 53 (2) (2006) 103–121.
[24] T. von Karman, (1929) The Impact of Seaplane During Landing. NACA TN 321.
[25] H. Wagner, Z. Angew. Math. Mech. 12 (1932) 193–215.
[26] S. Wang, C.G. Soares, Ocean Eng. 78 (2014) 73–88.
[27] G. Wei, (2005) A Fixed Mesh Method for General Moving Objects. Flow Science Technical Note #73 (FSI-05-TN73), Flow Science Inc.
[28] Q. Yang, W. Qiu, Ocean Eng. 43 (2012) 82–89.
[29] J.M. Yang, F. Stern, J. Comput. Phys. 228 (17) (2009) 6590–6616.
[30] Y. Zhang, Q. Zou, D. Greaves, D. Reeve, A. Hunt-Raby, D. Graham, P. James, X. Lv, Commun. Comput. Phys. 8 (2) (2010) 265–288.
[31] R. Zhao, O.M. Faltinsen, J. Fluid Mech. 246 (1993) 593–612.
[32] X. Zhu, O.M. Faltinsen, C. Hu, ASME J. Offshore Mech. Arct. Eng. 129 (4) (2007) 253–264.